

TEMPLATE-INDUCED CRYSTAL GROWTH

John W. White, A. Brown, K. Edler, S. Holt, J. Watson, P. Reynolds, J. Ruggles
Research School of Chemistry
The Australian National University
Canberra ACT 0200, Australia

and

L. Iton
Materials Science Division
Argonne National Laboratory
Argonne, USA

KEYWORDS: Biomineralisation, Silicate, Film

ABSTRACT

The process of "mineralisation" in biology leads to a diversity of inorganic structures based on silica or calcium carbonate. Some of these are composite and, at the same time, highly crystalline. In all cases a molecular or self assembled "template" species has been identified as the promoter for the crystallisation of the new structure. In biology these "templates" are the end step in the conveyance of genetic information to the inorganic synthesis and an understanding of how they work is the key to mimicking biomineralisation in the laboratory. The lecture will describe how modern scattering methods, using x-rays and neutrons, have revealed the very first steps in the process from the first association of the inorganic with the "template" in zeolite and mesoporous silicate syntheses in the bulk and at interfaces. We now have some control of the phase diagram at surfactant interfaces and novel nanoscale structures have been produced and quantitative thermodynamic information on the kinetics of growth between 20Å and 1000Å will be discussed. It now seems to be possible also to reproducibly create structure at the micron scale and the lecture will describe some of these developments.

INTRODUCTION

Part of the future of chemical physics is to understand and control the ways in which intermolecular forces give rise to the diversity of structure and dynamics in biological systems. Mimicking phenomena like biomineralisation, in particular the role of molecular templates as a basis for growing inorganic structures, and using modern synchrotron x-ray and neutron scattering shows the way to make a variety of new materials. The structures produced in this way appear on the nanometer scale, the tens of nanometer scale and the micron scale. As the objective of our work is to understand formation mechanisms and to control growth, the combined use of equilibrium thermodynamic properties and kinetic paths to metastable states is of interest.

MOLECULAR TEMPLATES

In nature, molecular or macromolecular templates such as poly l serine have been invoked as the structure directing agents in the organisation of silica to form the beautiful structures observed in diatoms^{1,2} and proteins made by molluscs appear to give rise to the colourful composite "nacre" of shells³. The calcium carbonate here is of almost single crystal quality interspersed with organic matter⁴. An example for the laboratory is the formation of the zeolite, Silicalite or ZSM-5 directed by the tetra n-propyl ammonium ion as template. We have found that the influence of this ion is great, even at the earliest stages of hydrothermal synthesis at room temperature both in the gel phase⁵ and from clear preparations^{6,7}. Homogeneous nucleation around the template ion can thus be followed from the scale of about two nanometres to microns⁷. Figure 1 shows the *in situ* x-ray small angle scattering from a clear solution synthesis mixture as a function of time of heating at 100C.

LIQUID CRYSTAL TEMPLATES - THE TENS OF NANOMETER SCALE

The production⁸ of mesoporous materials with internal structures in the tens of nanometer scale using surfactant liquid crystal mesophases as templates for silicate growth was a major step upward in the scale of structures that could be induced by templates. That the chemistry and structure^{9,10,11} may be optimised by improvements to the synthetic conditions^{12,13} continues to suggest new means of control the structure directing process by modifying the surfactancy, the direction of surfactant phase transitions and by imposing external constraints.

By constraining growth to a surface - the air liquid interface, highly crystalline one and two dimensional structures may be studied^{14,15}. The structural problem is greatly simplified and mesoporous films with considerable potential practical application are produced. The kinetics of this form of growth are admirably studied by the new methods of x-ray and neutron reflectivity.

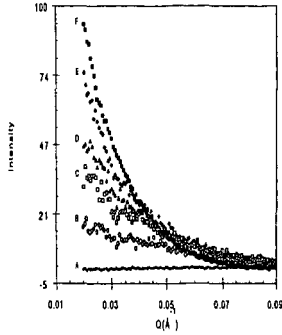


Figure 1. Small angle x-ray scattering patterns of the silicite solution after heating times of A) 0 min, B) 30 min, C) 60 min, D) 120 min, E) 360 min and F) 840 min.

Films may be grown^{14,16,17} by slowly hydrolysing tetra ethoxy silane in the presence of an aqueous surfactant solution at about ten times the critical micellar concentration. The kinetics show a prolonged induction phase where there is no visible film growth for five to ten hours and then a fairly rapid growth of film to thicknesses of about a few microns. Changing the conditions allows thicker or thinner films to be made. X-ray and neutron reflectivity methods allow these processes to be followed in real time and the subsurface structures to be worked out at each stage. In these methods¹⁸ the intensity of specularly reflected x-rays or neutrons is analysed for reflection angles above the critical angle for external reflection.

Figure 2 shows the x-ray specular reflectivity from the air-water interface at which a templated silica film is growing. In the "induction phase" (a,b) the reflectivity is clearly modified from that of water or a surfactant solution of the same strength as that of the cetyl trimethyl ammonium bromide used for the preparation. The bump in the reflectivity shows that there is a surface excess and treatment of the data indicates that this "embryo film" is about 27Å thick. Its growth up to the point where a film can be seen has been followed^{14,15}. The data contain a strongly falling (Q_z^{-4}) Fresnel component which may be removed by multiplying by Q^4 to show the Kiessig fringe - the form factor - of this surface layer. At longer times of reaction (b,c) a clear Bragg peak emerges showing that a highly ordered film structure has been created at the interface.

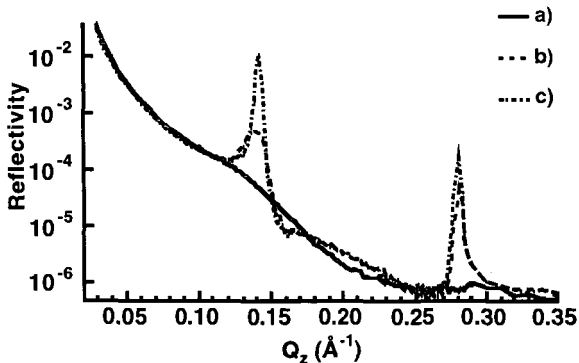


Figure 2. X-ray reflectivity from the air-water interface during the induction period showing the development of the reflectivity profile over time into diffraction peaks. a) 530 minutes, b) 608 minutes, and c) 687 minutes. The quality of the fits is shown.

Using neutron reflectivity and choosing deuterated and non deuterated surfactant against heavy water and air contrast matched water the contrast between the surfactant part and the silicate part of the film layer structure can be systematically varied¹⁵. In combination with the x-ray reflectivity results a complete picture of the development in one dimension, emerges. Figure 3 shows the Fresnel corrected reflectivity functions for several contrasts (left hand side) and the appropriately transformed real space densities at and below the growing surface at various times.

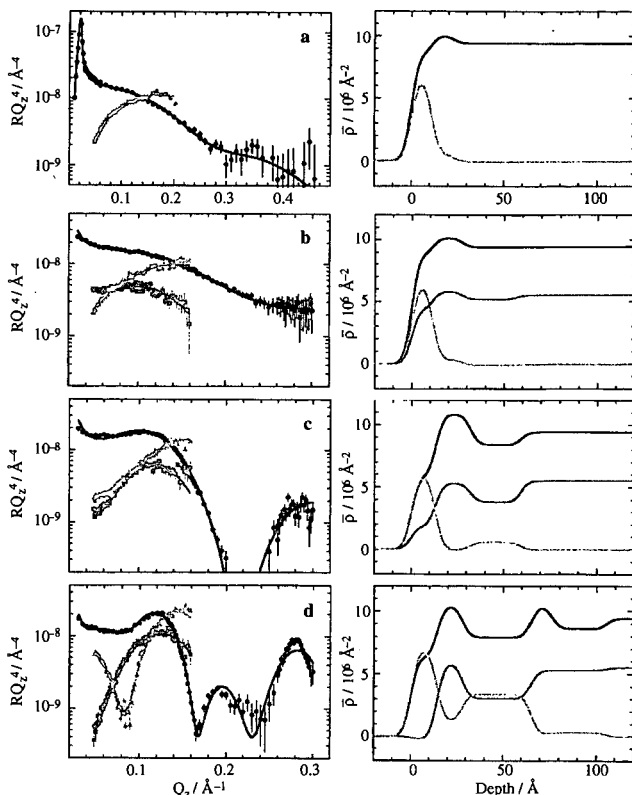


Figure 3. Fresnel corrected reflectivity profiles for both x-rays (black), deuterated surfactant on air contrast matched water (orange), and protonated surfactant on D_2O (blue) with the corresponding real space profiles for a growing silicate film at the air - water interface.

The real space model emerging from these data is of silicated, hexagonally arranged micelles lying parallel to the air-water interface as shown in Figure 4. Another aspect for the future comes from our recent work using x-ray and neutron reflectometry to study the induction phase for film growth and the origin of the hexagonally packed tubular micelle at apparently much lower concentrations of surfactant than would be expected for this phase in the pure surfactant. It now looks as though an anion induced phase transition from a glassy or cubic phase to the hexagonal occurs and that this may be controlled by chemical means¹⁹. A similar phenomenon has been observed by Aksay et al for calcium carbonate films templated by a porphyrin based surfactant²⁰.

MICRON SCALE STRUCTURES AND THE FUTURE

In experiments to improve our understanding of the chemistry behind the growth of three dimensional MCM-41 structures from cetyl trimethyl ammonium templated gels some remarkable structures on the micron scale were observed by transmission electron microscopy²¹ on the underside of the growing films. One of these is shown in Figure 5. Rod like, disc like and worm like structures were also recorded, some resembling the tactoids observed by Bernal and Fankuchen²² in tobacco mosaic virus solutions at concentrations above ca 1.5wt%. We and others^{17, 23} have recorded them frequently in film preparations such as those described above.

We suppose that such structures (particularly the worm-like structures) might be common in surfactant systems but are observable to us because that are "fossilised" by the silicate component and so are durable enough to see in the electron microscope. Clearly there is another length scale operating to form these structures. For example, inside the tactoids one can clearly see the ca 40Å diameter threads of the templated, silicated cylindrical micelles whose scale is determined by the surfactant size and silica coating. The balance of the surface and bulk energy created by such adhesion of tubules to form a tactoid bundle may provide the length scale determining the bundle size. That such structures might also be designed poses one of the fascinating future possibilities for the work described in this lecture.

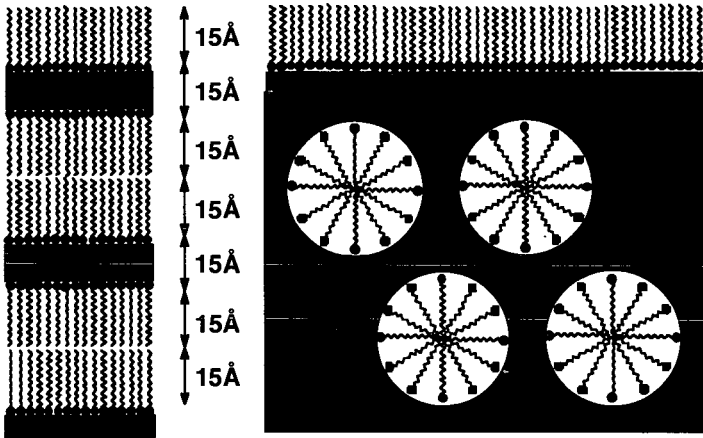


Figure 4. Model of the one dimensional structure at the air-water interface of a growing silicate film templated at 25°C by a cetyltrimethyl ammonium template.



Figure 5. Micron scale structure observed on the growing side of a silicate film templated by cetyltrimethyl ammonium bromide.

REFERENCES

1. R.E. Hecky *et al.*, *Marine Biology*, **19**, 326-330, (1973).
2. Chia-Wei Li and B.E. Volcani, *Protoplasma*, **124**, 10-29, (1985).
3. B.L. Smith, *Chemistry and Industry*, 17 August, 649-653 (1998).
4. X. Shen, A.M. Belcher, P.K. Hansma, G.D. Stucky and D.E. Morse, *J. Biol. Chem.*, **272**, 32472-32481, (1997).
5. T.O. Brun, J.E. Epperson, S.J. Henderson, L.E. Iton, F. Trow and J.W. White *Langmuir*, **8**, 1045-1048, (1992).
6. J.N. Watson and J.W. White, *Chemical Communications*, 2767-2768, (1996).
7. J.N. Watson, L.E. Iton, R.I. Keir, J.C. Thomas, T.L. Dowling and J.W. White *Journal of Physical Chemistry B*, **101**(48), 10094-10104, (1997).
8. Beck, J. S., Vartuli, J. C., Roth, W. J., Leonowicz, M. E., Kresge, C. T., Schmitt, K. D., Chu, C. T.-W., Olson, D. H., Sheppard, E. W., McCullen, S. B.; Higgins, J. B. and Schlenker, J. L., *J. Am. Chem. Soc.*, **114**, 10834, (1992).
9. G.D. Stucky, A. Monnier, F. Schüth, Q. Huo, D. Margolese, D. Kumar, M. Krishnamurthy, P. Petroff, A. Firouzi, M. Janicke and B.F. Chmelka, *Mol. Cryst. Liq. Cryst.*, **240**, 187, (1994).
10. K.J. Edler and J.W. White, *J. Chem. Soc. Chem. Commun.*, 155-156 (1995).
11. D. Cookson, K.J. Edler, P.A. Reynolds and J.W. White, *Journal of the Chemical Society, Faraday Transactions*, **93**, 199-202 (1997).
12. R. Ryoo, and J.M. Kim, *J. Chem. Soc., Chem. Commun.*, **711** (1995).
13. K.J. Edler, P.A. Reynolds, D. Cookson and J.W. White, *Chemistry of Materials*, **9**, 1226-1233, (1997).
14. A.S. Brown, S.A. Holt, Thien Dam, M. Trau and J.W. White, *Langmuir*, **13**(24), 6363-6365, (1997).
15. A.S. Brown, S.A. Holt, P.A. Reynolds, J. Penfold and J.W. White, *Langmuir*, **14** (19), 5532-5538, (1998).
16. I.A. Aksay, M. Trau, S. Manne, I. Honma, N. Yao, L. Zhou, P. Fenter, P.M. Eisenberger, S.M. Gruner, *Science*, **273**, 892 (1996).
17. H. Yang, N. Coombs, G.A. Ozin, *Journal of Materials Chemistry*, **8**, 1205 (1998).
18. J. Penfold, R.M. Richardson, A. Zarbakhsh, J.R.P. Webster, D.G. Bucknall, A.R. Rennie, R.A.L. Jones, T. Cosgrove, R.K. Thomas, J.S. Higgins, P.D.I. Fletcher, E. Dickinson, S.J. Roser, I.A. McLure, A.R. Hillman, R.W. Richards, E.J. Staples, A.N. Burgess, E.A. Simister and J.W. White, *J. Chem. Soc., Faraday Trans.*, **93**(22), 3899-3917, (1997).
19. J.L. Ruggles*, S.A. Holt, P.A. Reynolds and J.W. White. Submitted to *Langmuir*, (1999).
20. G. Xu, N. Yao, I.A. Aksay and J.T. Groves, *J. Amer. Chem. Soc.*, **120**, 11977-11985, (1998).
21. K.J. Edler, J. Dougherty, R. Durand, L. Iton, G. Kirton, G. Lockhart, Z. Wang, R. Withers and J.W. White, *Colloids and Surfaces*, **102**, 213-230 (1995).
22. J.D. Bernal and I. Fankuchen, *J. Gen. Physiol.*, **25**, 111, (1941).
23. M. Trau, Private Communication (1998).

APPLICATIONS OF X-RAY AND NEUTRON METHODS TO POROUS MANGANESE OXIDE SYSTEMS

Steven L. Suib¹, Wei Tong¹, Stephanie L. Brock², Jaya Nair², Volker Urban³, and Pappannan Thiyagarajan³

¹Department of Chemistry, University of Connecticut, U-60, Storrs, CT 06269-3060, ²Department of Chemistry, Wayne State University, 5101 Cass Avenue, Detroit, MI 48202, ³Intense Pulsed Neutron Source Division, Argonne National Laboratory, 9700 South Cass Avenue, Argonne, Illinois 60439

KEYWORDS: manganese oxides, crystallization, small angle neutron scattering (SANS)

ABSTRACT

This presentation will focus on the use of X-ray and neutron methods for studying various microporous and mesoporous manganese oxide materials. The manganese oxide systems crystallize as either layered or tunnel structure systems. The initial stages of nucleation and structural phase changes that occur during aging and thermal treatment will be discussed. Both diffraction and scattering methods have been used in these systems. Complementary characterization methods include surface area, pore size distribution, scanning electron microscopy, and high resolution electron microscopy experiments.

INTRODUCTION

The synthesis of quantum size¹ porous semiconducting^{2,3} manganese oxides has been accomplished by systematically varying the nature of organic cations which are used as structure directors.⁴ One of the major precursors for preparation of manganese oxide materials is KMnO_4 , which readily reacts with organic cations. This facile set of reactions has inhibited the synthesis of porous manganese oxides that contain organic moieties. We have focused on new synthetic routes to porous manganese oxides in the absence of inorganic cations. Stable colloids of layered manganese oxide materials can be prepared from reduction of tetraalkylammonium (tetramethylammonium, tetraethylammonium, tetrapropylammonium and tetrabutylammonium) permanganate salts. Such systems are interesting because particle size can be controlled, the colloids are extremely stable at room temperature, a variety of crystalline materials can result, and the initially formed phases can be interconverted into other phases. The particle sizes can be controlled from about 15 to 200 Å which allows systematic studies of nanocrystalline phase materials. Several aspects of these materials will be discussed including synthesis, characterization, and potential applications. Other related materials that have been prepared by using surfactants in order to generate mesoporous materials will also be described. The primary methods that have been used to understand these materials are X-ray powder diffraction and small angle neutron scattering methods.

EXPERIMENTAL

Samples were prepared by pipetting small amounts of the colloidal sol onto glass slides with concomitant evaporation of solvent prior to thin film formation, or by spreading thin layers of the sol onto glass slides. A Scintag XDS-2000 diffractometer with CuK_α radiation was used to obtain diffraction data. SANS data were collected on the time-of-flight small-angle diffractometer (SAD) at the Intense Pulsed Neutron Source (IPNS) at Argonne National Laboratory.

RESULTS AND DISCUSSION

X-ray diffraction (XRD) methods were used to study the phases that formed during synthesis of the colloids and subsequent production of gels and heated gels. XRD patterns of various tetraalkylammonium cations reacted with permanganate led to production of well ordered systems after thermal treatment. The mesoporous materials typically produced broad diffraction data so that lattice parameters and structural models were developed with electron diffraction data from transmission electron microscopy methods.

The XRD data clearly show that expanded octahedral layer (OL) synthetic birnessite materials (OL-1) were produced in all cases. The originally formed colloids before heating were quite amorphous whereas thermal treatment even at mild temperatures (such as 70°C) led to production of well ordered phases.

Small angle neutron scattering (SANS) experiments clearly show that small nanoclusters of manganese oxide are formed at initial stages of reaction. We have used this information to stop the growth of such nanoclusters in order to use various size species to prepare other systems. By using SANS data for sols heated and aged to different extents it has been possible to prepare clusters of various sizes. Further support for the varying sizes of such clusters comes from UV-visible spectroscopy where growth of the clusters leads to a red shift in absorbance.

The interlayer structure of these materials shows that about 3 major types of structures can form. One structure involves intercalation of only the tetraalkylammonium cations in between the layers. Another structural type involves incorporation of the tetraalkylammonium cations as well as one layer of water molecules which increases the d-spacing between these layers. A further increase in d-spacing occurs when 2 different water layers are incorporated with the tetraalkylammonium cations in between the layers of OL-1.

The shapes of the colloids can be determined by modeling the SANS data. Several shapes were proposed and the best fit to the data analysis is a layered phase similar to OL-1. These layered disks are believed to be precursors for most of the octahedral molecular sieve (OMS) and octahedral layered materials of porous manganese oxides that have been prepared.⁵ Several other factors are in line with this observation. First of all, the most common mineral of manganese oxide is the layered structure birnessite. Synthetic birnessite with small particle sizes is OL-1, which seems to always form in syntheses of OMS and OL materials. Secondly, calorimetric studies⁹ also suggest that birnessite and OL materials have lower heats of formation than any other porous or nonporous manganese oxide mineral or synthetic material.

The mesoporous manganese oxide systems that have been prepared also seem to grow from this initial layered phase.^{7,8} Certainly other factors are important in such syntheses such as the average oxidation state of manganese, the nature of the surfactant used in the synthesis, and the solvent.

The average manganese oxidation state in these systems is often around 3.6 or 3.7 as determined by titration and X-ray absorption studies. The reduction of Mn^{4+} to Mn^{3+} and Mn^{2+} leads to mixed valency, which in turn gives rise to enhanced conductivity of these materials. The semiconducting nature of these particulates allows experiments where charging problems can occur to be done more readily. Some examples include surface analyses by Auger electron spectroscopy, X-ray photoelectron spectroscopy and morphological studies by scanning and transmission electron microscopy. Such morphological studies have confirmed the generation of layered structures, although at times fibrous structures can be observed.^{4,8}

CONCLUSIONS

XRD and SANS studies have provided a wealth of information about porous manganese oxide materials such as the nature of the size and shape of particulates, stability, thermal effects, and the mechanism of crystal growth. Such studies are in line with the generation of layered nanoclusters of manganese oxide similar to birnessite, which can grow and aggregate into other structures.

REFERENCES

1. Steigerwald, M. L.; Brus, L. E. *Acc. Chem. Res.* **1990**, *23*, 183-188.
2. Zhang, L.; Coffer, J. L.; Xu, W.; Zerda, T. W. *Chem. Mater.* **1997**, *9*, 2249-2251.
3. Counio, G.; Esnouf, S.; Gacoin, T.; Boilot, J.-P. *J. Phys. Chem.* **1996**, *100*, 20021-20026.
4. Brock, S. L.; Sanabria, M.; Suib, S. L.; Urban, Thiyagarajan, Potter, D. I., *J. Phys. Chem.*, **1999**, in press.
5. Suib, S. L., *Curr. Op. Sol. State Chem.*, **1998**, *3*, 63-70.
6. Fritsch, S.; Post, J. E.; Suib, S. L.; Navrotsky, A., *Chem. Mater.*, **1998**, *10*, 474-479.
7. Tian, Z. R.; Tong, W.; Wang, J. Y.; Duan, N.; Krishnan, V. V.; Suib, S. L., *Science*, **1997**, *276*, 926-930.
8. Luo, J.; Suib, S. L., *J. Chem. Soc. Chem. Comm.*, **1997**, 1031-1032.

Jerry E. Hunt, Langqiu Xu, Randall E. Winans, and S. Seifert
Chemistry Division
Argonne National Laboratory
9700 South Cass Ave.
Argonne, IL 60439

KEYWORDS: small angle X-ray scattering, sieving, separation, MCM

ABSTRACT

We have studied the temperature stability of M41S class siliceous mesoporous materials loaded with carbonaceous material by temperature programmed small-angle X-ray scattering (TPSAXS) techniques. Results show the thermal structural instability of large pore pure silica sieve material with carbonaceous material (such as coal extracts) occluded within the pores of mesoporous 31 Å M41S materials. Unfilled pore M41S materials do not show thermal-related structural instability.

INTRODUCTION

Mesoporous silicates are attractive candidates for separations and applications in catalysis due to their high surface areas and highly ordered mesoporous (20-100Å) nature. MCM-41 is one member of a family of highly uniform mesoporous silicate materials introduced by Mobil, whose pore size can be accurately controlled in the range 1.5 Å-10 nm.^{1,2} This recently discovered class of zeolites, more generally called, M41S, should be useful to effect size separation, act as hosts to nanoclusters, and as shape selective separation media, due to their large pore sizes. True molecular sieving on the size range of molecular and cluster types found in aggregating solutions should be possible with M41S materials by tuning the pore size.

The thermal stability is of crucial importance to the practical application of these mesoporous materials. Few reports of the thermal stability of these mesoporous materials are in the literature. Pure silica M41S is stable when heated to 850°C in air or 800°C in air with low water vapor pressure.³ However, the mesoporous structure collapses when mechanically compressed or when exposed to water vapor for long periods at room temperature.⁴ There are enormous efforts devoted to improving the stability of these materials.

In the present investigation, we have synthesized mesoporous silicate materials with a surface area of approximately 1100 m²/g and pore sizes of approximately 25 Å and 31 Å. The subject of this paper is the study of the temperature stability of these pore filled mesoporous materials as measured by small angle X-ray scattering.

EXPERIMENTAL

The SAXS instrument was constructed at ANL and used on the Basic Energy Sciences Synchrotron Radiation Center CAT undulator beamline ID-12 at the Advanced Photon Source.

Monochromatic X-rays (8.5–23.0 keV) are scattered off the sample and collected on a 19 x 19 cm² position sensitive two-dimensional gas detector. More recent data are taken using a 9-element mosaic CCD detector (15 x 15 cm) with maximum resolution of 3000 x 3000 pixels. An advantage of this new detector is that unlike the wire detector, the full beam for the undulator can be used, which gives a factor of 1000 increase in intensity. The scattering intensity has been corrected for absorption, the empty capillary scattering, and instrument background. The differential scattering cross section has been expressed as function of the scattering vector q , which is defined as $q = (4\pi/\lambda) \sin \theta$, where λ is the wavelength of the X-rays and θ is the scattering half-angle. The value q is proportional to the inverse of the length scale (Å⁻¹). The instrument was operated with a sample-to-detector distance of 68.5 to obtain data at $0.03 < q < 0.7 \text{ Å}^{-1}$.

A quartz capillary heating apparatus was constructed to obtain a controlled heating rate under an inert atmosphere of nitrogen for in situ SAXS measurements. Quartz capillaries (1 mm) were used to sample 1 mg of M41S material. Scattering patterns were obtained as the sample is heated from 25-600 °C under a nitrogen flow system at a rate of approximately 25°/minut.

Synthesis of MCM-41 was an approach combining the advantages of several literature works.^{2,3,5} Different chain length of surfactants, ranging from dodecyltrimethylammonium to octadecyltrimethylammonium bromide, were used as a template to construct a periodic mesophase. The silica source used was tetramethyl orthosilicate. The synthesis was carried out at room temperature in the solution of methanol and sodium hydroxide mixture. The materials were annealed at 600 °C. Pure silica versions of these zeolites were prepared to alleviate irreversible absorption by aluminum sites.

X-ray diffraction (XRD) analyses were carried out on a Rigaku Miniflex+ instrument using $\text{CuK}\alpha$ radiation, a NaI detector, a 0.05° step size, and a 0.50°, 2/min scan rate. XRD and SAXS showed pore sizes of 25 Å and 31 Å for the two M41S-class zeolites.

A pyridine extract of mv bituminous Upper Freeport coal (APCS 1) of the Argonne Premium Coal Samples series was divided and stirred for one week in 31 Å and 25 Å M41S material. After filtering, the zeolite material containing the coal was extracted with methylene chloride. Approximately 25% of the coal material was recovered from each zeolite by methylene chloride extraction. Further extraction with chlorobenzene resulted in only a few additional percent of coal.

TGA-DTA (thermal gravimetric analysis and differential thermal analysis) measurements were obtained on a SDT 2960 from TA Instruments. These samples were measured against an alumina standard in a 100 mL/min O_2 flow with a temperature ramp of 10°C/min to 800°C. The TGA data is also represented in its first-derivative or differential thermal gravimetry (DTG) format. Total organic loss were calculated by measuring the weight loss over the approximate temperature range of 200-600 °C.

RESULTS AND DISCUSSION

Small angle X-ray scattering

A typical plot of the scattering data for the two pore sizes of M41S material is shown in Figure 1. At low q ($< 0.04 \text{ \AA}^{-1}$), scattering arises from the whole particle. This scattering can be related to information about the particle size, composition, and, ultimately, surface texture. The Bragg diffraction peaks give information about the internal structure of the particles, defining the nature, and packing dimensions of the channel in the mesoporous materials. The curves clearly show relatively narrow Bragg diffraction peaks associated with the hexagonal lattice. The lattice spacing d is 25 Å and 31 Å for the two materials synthesized. The relatively narrow diffraction peaks indicate good crystalline structure. The acquisition time for each data set was 0.1 sec.

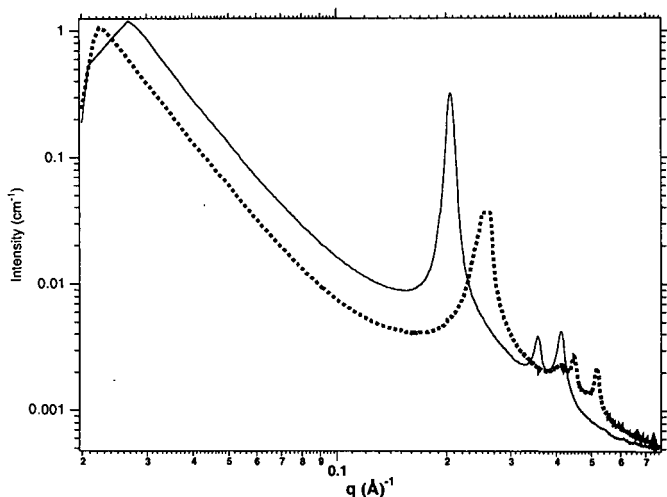


Figure 1. The small-angle X-ray scattering from 25 Å (dotted line) and 31 Å (solid line) M41S mesoporous silicate materials.

In the TPSAXS experiments, the M41S materials retain their structure even at temperatures as high as 650 °C.

When the void spaces in the M41S materials were filled with pyridine extracts from coal, the scattering is quite similar to the unfilled materials. This can be seen in comparing Figure 1 with the room temperature scattering of Figures 2 and 3. The extracts are expected to contain clusters of organic molecules which fill the pores of the M41S materials.

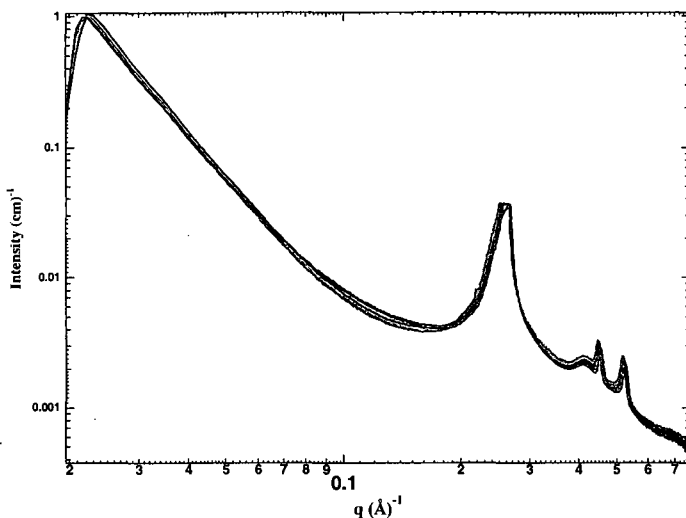


Figure 2. The temperature programmed small-angle X-ray scattering of coal extract imbibed in 25 Å M41S mesoporous material. The temperature range is from 25 °C to 600 °C.

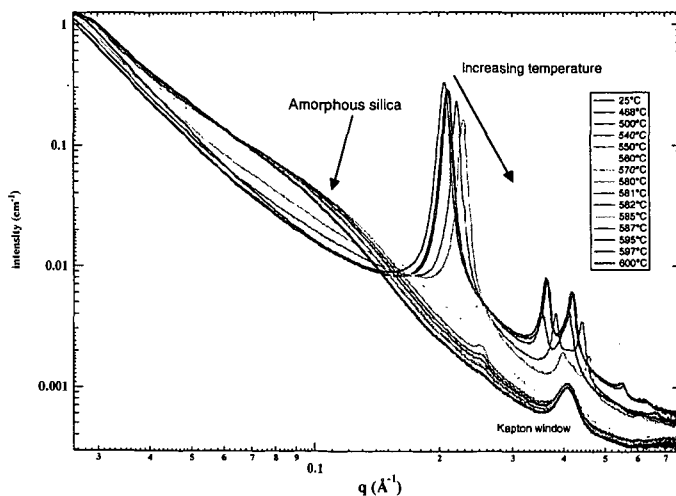


Figure 3. The temperature programmed small-angle X-ray scattering of coal extract imbibed in 31 Å M41S mesoporous material. The temperature range is from 25 °C to 600 °C.

Figure 2 shows that the mesoporous structure for the 25 Å material is maintained throughout the temperature range of 25-600 °C. The scattering is dominated by the mesoporous material and remains essentially unchanged over the entire temperature range. We used TGA to determine the weight loss as a function of temperature. From this data we can determine the total amount of organic material in the mesoporous zeolite. The TGA data shows a weight loss per cent of the total sample weight of 15.6% for the 25 Å material. The TGA indicates that very low molecular weight material is evolved at about 60 °C, which we assign to occluded pyridine. The major part of the organic material begins to come off at roughly 300 °C and peaks at 500 for the 25 Å material. In addition, there is a distinct shoulder at 520 in the 25 Å which may indicate different organic compounds or clusters of compounds.

The TPSAXS data for the 31 Å material is shown in Figure 2. The most striking feature of this data is the clear structure collapse of the mesoporous material. The 31 Å material rapidly collapses beginning around 475 °C as indicated by the decreasing Bragg diffraction peak. At the same time a large hump appears around 0.08 Å⁻¹, which we assign to amorphous silica. The structure collapses completely at 600 °C to what appears to be an amorphous silica phase. The 31 Å pore size material contains a larger amount of coal extract from the pyridine solution 22.6% for the 31 Å material versus 15.6 % for the 25 Å M41S mesoporous material. In the TGA analysis the major part of the organic material begins to come off at roughly 300 °C and peaks at 440 °C for the 31 Å material. In addition, there is a distinct shoulder at 460 in the 31 Å that may correspond to different organic compounds or clusters of compounds. A peak at 675 in the 31 Å material is only 1.5% of the total weight, but may be related to very tightly bound (very polar) organic material on the silica.

Certainly, very polar material from the coal extracts will bind to the silica. For both M41S mesoporous materials, only 25% can be removed from the zeolite by washing. The more nonpolar materials will be preferentially extracted in the washes of coal-infused M41S material leaving more tightly bound polar compounds. Mass spectrometry results show some differences in the nature of organic material in the two M41S materials. The 31 Å material has larger aromatic ring sizes than the 25 Å material.⁶

Clearly, the lower molecular weight materials (such as residual pyridine and other lower boiling point compounds) that are evolved from the M41S materials do not affect the ordered structure. However, at higher temperatures, the 31 Å material begins to decompose, while the 25 Å remains stable. There are two possibilities to consider. First, if the forces associated with thermal decomposition of the organic material are the same, then the larger pore material is less stable than the smaller. Alternatively, because data suggests that there are differences in the organic material structure, quantity, and the decomposition of the organic material, the 31 Å material may experience more stress on the structure than the 25 Å material, resulting in complete destruction of the larger mesoporous material. Further investigation of the surface structure of the mesoporous using TPSAXS is planned.

ACKNOWLEDGMENT

This work was performed under the auspices of the Office of Basic Energy Sciences, Division of Chemical Sciences, U.S. Department of Energy, and use of the Advanced Photon Source was supported by BES-DOE, all under contract number W-31-109-ENG-38. The support of the BESSRC staff is appreciated, especially J. Linton, M. Beno, G. Jennings, and M. Engbretson.

REFERENCES

1. Beck, J. S., U.S. Pat., No. 5,057,296, 1991
2. Beck, J. S.; Vartuli, J. C.; Roth, W. J.; Leonowicz, M. E.; Kresge, C. T.; Schmitt, K. D.; Chu, C. T.-W.; Olson, D. H.; Sheppard, E. W.; McCullen, J. B.; Higgins, J. B.; Schlenker, J. L., *J. Am. Chem. Soc.*, 1992, 114, 10834-43
3. Chen, C. Y.; Li, H. X.; Davis, M.E. *Microporous Mater.* 1993, 2, 17
4. For example, Tatsumi, T.; Koyano, K. A.; Tanaka, Y.; Nakata, S. *Chem. Lett.* 1997, 469.
5. Pinnavaia, T. J.; Thorpe, M. F., *Access in Nanoporous Materials*, Plenum Press: New York, 1995.
6. Hunt, J. E.; Winans, R. E.; Ahrens, M.; and Xu, L. *Prepr. Pap. - Am. Chem. Soc., Div. Fuel Chem., 218th ACS National Meeting, New Orleans, Aug. 22-26, 1999*, pp. 610-613.

THE CRYSTALLIZATION OF HECTORITE CLAY AS MONITORED BY SMALL ANGLE X-RAY SCATTERING AND NMR

K. A. Carrado*, L. Xu, S. Seifert, D. Gregory, K. Song, R. E. Botto
Chemistry Division 200, Argonne National Laboratory
9700 South Cass Avenue, Argonne, IL 60439

KEYWORDS: clay, crystallization, small angle x-ray scattering (SAXS)

ABSTRACT

We have probed the 48-hr crystallization of a magnesium silicate clay called hectorite. Small angle x-ray scattering (SAXS) at the Advanced Photon Source using aliquots ex situ has revealed that data is consistent with ex situ XRD, TGA, AFM, and IR data in that all these techniques see clay crystallites beginning to form in the first few hours of reaction. Tetraethylammonium (TEA) ions are used to aid crystallization and become incorporated as the exchange cations within the interlayers. ^{13}C NMR shows that 80% of the final TEA loading is accomplished in the first 10 hrs. ^{29}Si NMR displays a visible clay silicate peak after just 1 hr. In addition, the first in situ study of clay crystallization of any kind was performed by in situ SAXS. Results are consistent with the ex situ data as well as showing the sensitivity of SAXS to sol gel reactions occurring on the order of minutes.

INTRODUCTION

The mechanism of formation of clays is of interest because of the use of synthetic layered silicates as heterogeneous catalyst supports and in various other technological applications. We have probed the crystallization of a magnesium silicate clay called hectorite by several ex situ (samples isolated after progressive crystallization times) techniques. For complete crystallization, heating for 48 hours at 100°C is needed. However, several techniques have revealed that significant clay growth occurs in the first few hours of hydrothermal treatment. Evidence of clay peaks in XRD occurs after just 4 hours of hydrothermal treatment, and $\text{Mg}(\text{OH})_2$ is no longer observable by XRD after 14 hours; observable changes in DTG and IR occur at about 4-6 hours as well [1]. From AFM results [2], Ostwald ripening is apparent in this system in certain time frames. Most noticeably at 4 hours but still at 8 hours, nucleation of the clay crystallites is occurring. Between 8 and 14 hours, the nucleation is complete, as evidenced by the unimodal distribution of lengths and heights in the 14 hour sample. At times longer than 14 hours, particles appear to simply coalesce and form substantially larger aggregate particles. We have now exploited both small angle x-ray scattering (SAXS) and solid state NMR to access different size regimes, length scales, and timeframes, to add information to the overall scenario of a clay crystallization mechanism.

EXPERIMENTAL

The typical method for in situ hydrothermal crystallization of organo-hectorite clays is to create a 2 wt% gel of silica sol, magnesium hydroxide sol, lithium fluoride, and organic in water, and to reflux for 2 days. Complete details can be found elsewhere [1-3]. Reagents were purchased from Aldrich. The organic of choice for crystallization studies is tetraethylammonium chloride (TEA). Precursor clay gels are of the composition:



to correlate with the ideal hectorite composition [4] of $\text{Ex}_{0.66}[\text{Li}_{10.66}\text{Mg}_{5.34}\text{Si}_8\text{O}_{20}(\text{OH},\text{F})_4]$, where Ex = exchangeable cation (Ex = Li, TEA from this gel). A typical (scaled-down) reaction begins by dissolving 0.72 mmol of TEA in water and adding 4.8 mmol LiF with stirring. Separately, 24 mmol $\text{MgCl}_2 \cdot 6\text{H}_2\text{O}$ is dissolved in water and mixed with 32 ml of 2 N NH_4OH to crystallize fresh $\text{Mg}(\text{OH})_2$. Prior to use, this brucite source must be washed several times with water to remove excess ions. It is then added wet to the organic-LiF solution. This slurry is stirred for about 15 minutes before addition of 0.036 mol silica sol (Iudox HS-30, Na^+ -stabilized, 30%). This mixture is refluxed for up to 48 hr then centrifuged and the products are washed and air-dried. Small aliquots for ex situ time-resolved studies are removed at various times during the crystallization.

The SAXS instrument was constructed at ANL and used on the Basic Energy Sciences Synchrotron Radiation Center CAT undulator beamline ID-12 at the Advanced Photon Source [5,6]. For ex situ powder studies, the same powders as were used for the NMR analyses were sprinkled onto and sealed in scotch tape "cells". For the ex situ gel studies, wet aliquots were concentrated (via centrifugation) and transferred to 1.5 mm quartz capillaries. The SAXS data were collected in 5 minutes exposures (scans). Controls of pure silica and brucite sols (diluted to appropriate concentrations) were also run in

capillaries. For the in situ study, a small portion of unreacted clay gel was transferred to a 1.5 mm quartz capillary and sealed (the gel was first pre-concentrated by 75%). This capillary was placed in a home-built furnace assembly such that the gel was directly in the beam path. Temperature was computer-controlled; scanning began at 70°C, which took only 3-4 minutes to reach. Within 5 minutes the temperature had reached 100°C and held at $\pm 1^\circ\text{C}$ for the duration of the run. SAXS data were collected in 2 min scans divided by 5 μsec for the first 2 hrs, then as 10 min scans for the remaining 10 hrs. Monochromatic x-rays at 10.0 keV were scattered off the sample and collected on a $19 \times 19 \text{ cm}^2$ position sensitive two-dimensional gas detector. The scattered intensity has been corrected for absorption, scattering from a blank capillary containing only water (or scattering from blank scotch tape for the powder studies), and instrument background. The differential scattering cross section can be expressed as a function of the scattering vector Q , which is defined as: $Q = 4\pi (\sin \theta) / \lambda$, where λ is the wavelength of the x-rays and θ is the scattering half angle. The value of Q is proportional to the inverse of the length scale (\AA^{-1}). The instrument was operated at a sample-to-detector distance of 67.0 cm to obtain data at $0.04 < Q < 0.7 \text{ \AA}^{-1}$. Mylar windows were used because mylar does not have diffraction peaks in this Q range.

NMR data were acquired on a Bruker Advance DSX-200 spectrometer operating at a ^{13}C Larmor frequency of 50.3 MHz. A Bruker 7mm MAS probe and a simple 90° -pulse-acquire experiment was used for all experiments. Sample spinning was maintained at $4000 \pm 2 \text{ Hz}$. Data were acquired in the presence of proton decoupling with proton power set to 80 kHz. The 90° -pulse times were 6.5 and 7.0 μs for ^{13}C and ^{29}Si , respectively. Recycle delays were 3 and 200 sec for ^{13}C and ^{29}Si experiments respectively. The number of transients recorded were 2400 and 128 for ^{13}C and ^{29}Si spectra, respectively. All spectra were referenced to TMS. Hexamethylbenzene was used as a secondary reference for ^{13}C spectra, and TKS was used as a secondary reference for ^{29}Si spectra [7]. All samples were packed to the same level in the rotor. However, because of variations in density, the sample weight varied from 114 to 153 mg. Thus, the data points in Figure 4 were normalized by weight. No attempt was made to normalize the spectra in the stacked plot (Figure 3).

RESULTS AND DISCUSSION

Results from SAXS using aliquots ex situ show, first, that data for both isolated dried powders and the wet gels are consistent with each other. This has implications for SAXS sample preparation in that, for convenience, either form (wet or dry) can be used. Figure 1 shows the data from the gels. Scattering from the starting material silica sol (seen at about 0.08 \AA^{-1}) gradually disappears as the clay crystallizes and scatters in the basal spacing region (0.4 \AA^{-1} , 15 \AA). This phenomenon is visibly evident at about 6 hrs. High background levels in this high- q region that are probably due to brucite scattering (as seen in the control sample that was measured) disappear sooner, between 1 and 4 hrs. This data is consistent with ex situ XRD, TGA, and IR data in that all these techniques see clay crystallites beginning to form after about 4 hrs of reaction.

In addition, the first in situ study of clay crystallization of any kind was performed by in situ SAXS. These data are shown in Figure 2 with only a few representative curves displayed. Results are consistent with the ex situ data. There is background scatter in this high- q basal spacing region well past the 4 hr point in at which it disappears for ex situ samples. It is suspected that this is due to the overall weak intensity of the signal due to a low concentration of clay in the beam (note the low intensity at $q = 0.04 \text{ \AA}^{-1}$, especially as time progresses).

Tetraethylammonium (TEA) ions are used to aid crystallization, and they become incorporated as the exchange cations within the interlayers. Figure 3 displays the ^{13}C NMR plots of several powder aliquots with the methyl and methylene peaks of TEA clearly growing in with time. In fact, this technique is so sensitive that in as little as 30-60 minutes there is enough TEA incorporation to be visible. A plot of the normalized signal (by weight) with reaction time shows that 80% of the final TEA loading is accomplished in the first 10 hrs (see Figure 4), after which the incorporation occurs at a much slower rate. This is in agreement with AFM results [2], where Ostwald ripening is apparent in this system only in certain time frames. Most noticeably at 4 hours but still at 8 hours, nucleation of the clay crystallites is occurring. Between 8 and 14 hours, the nucleation is complete, as evidenced by the unimodal distribution of lengths and heights in the 14 hour sample. At times longer than 14 hours, particles appear to simply coalesce and form substantially larger aggregate particles. ^{29}Si NMR displays a visible clay silicate peak after just 1 hr, which increases as the silica peak decreases up to 48 hrs (figure not shown).

CONCLUSIONS

The ^{13}C NMR data presented here has allowed us to nearly pinpoint the time at which clay crystallites stop nucleating and begin to simply accrete and coalesce. Previous AFM studies had indicated that this occurred between 8 and 14 hours for the hectorite system. After 10 hours, ^{13}C NMR shows that 80% of the TEA has been incorporated in a linear fashion. This may mean that just one mechanism is active during the early stages of nucleation and crystallization. Between 10 and 14 hours there is a clear break in the NMR data of TEA uptake, after which AFM has shown that primarily agglomeration of particles is taking place. The SAXS data are in agreement with all other methods in terms of visible tracking of clay nuclei. The in situ SAXS data, since they are in agreement with ex situ data, confirm that vital information is not lost by isolating aliquots at various times for analysis. In addition, careful analysis of these SAXS curves in the future should yield information on changes occurring on the timescale of minutes.

ACKNOWLEDGEMENTS

R. E. Winans, M. Beno, and J. Linton of ANL are recognized for their help with various SAXS experimental details, as are P. Thiyagarajan and K. Littrell of ANL for devising the SAXS data analysis packages. J. Gregar of ANL sealed the SAXS sample cells for in situ heating. This research was performed under the auspices of the U.S. Dept. of Energy, Office of Basic Energy Sciences, Division of Chemical Sciences under contract number W-31-109-ENG-38, and benefitted from the use of the APS at ANL.

REFERENCES

1. K. A. Carrado, P. Thiyagarajan, K. Song, "A study of organo-hectorite clay crystallization", *Clay Minerals* **1997**, *32*, 29-40.
2. K. A. Carrado, G. W. Zajac, K. Song, J. R. Brenner, "Crystal growth of organo-hectorite clay as revealed by atomic force microscopy", *Langmuir* **1997**, *13*, 2895-2902.
3. K. A. Carrado, "Synthetic organo- and polymer-clays: preparation, characterization, and materials applications", *Applied Clay Science* **1999**, in press.
4. R. E. Grim, *Clay Mineralogy*, 1968. McGraw-Hill: NY, p. 68.
5. R. E. Winans, S. Seifert, P. Thiyagarajan, "Time resolved small angle x-ray scattering reactivity studies on coals, asphaltenes, and polymers", *Am. Chem. Soc. Div. Fuel Chem. Prepr.* **1999**, *44*, 576-580.
6. For a full description of the instrument see <http://www.bessrc.aps.anl>.
7. J. V. Muntean, L. M. Stock, R. E. Botto, "Tetrakis(trimethylsilyl) silane: a suitable standard for solid state NMR spectroscopy", *J. Magn. Reson.* **1988**, *76*, 540-542.

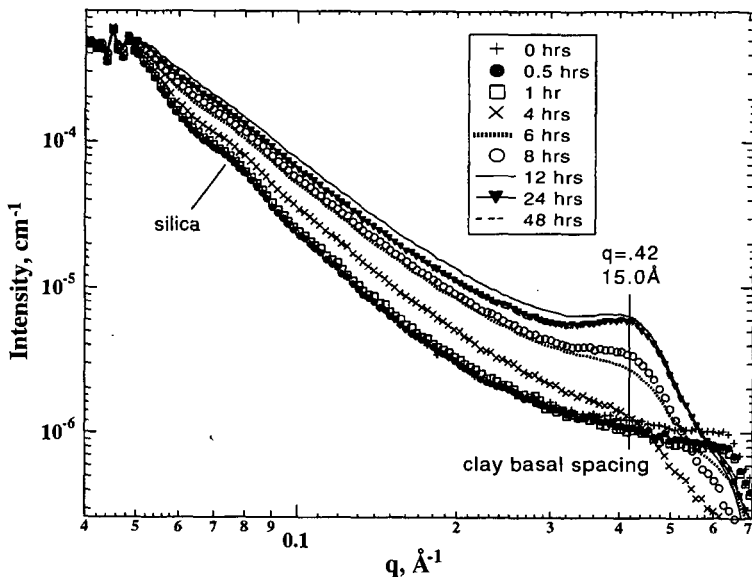


Figure 1. SAXS of ex situ synthetic TEA-hectorite gel aliquots taken at various times indicated in the legend.

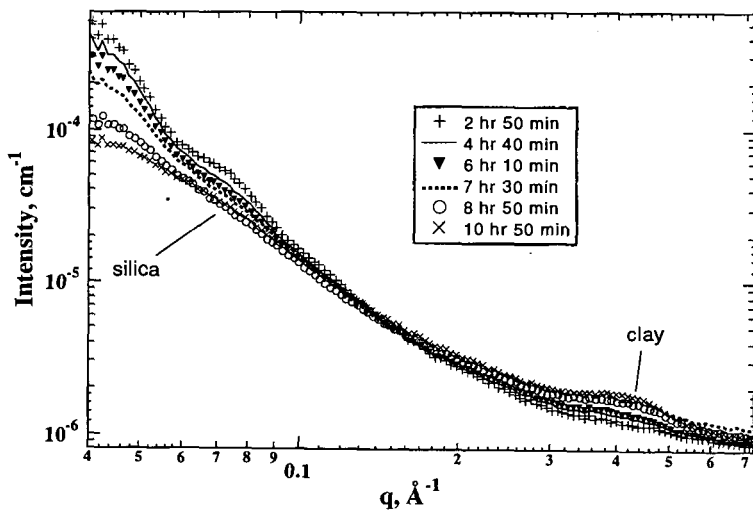


Figure 2. SAXS of in situ TEA-hectorite gel during crystallization at early stages. Only a few selected plots are shown for clarity as detailed in the legend.

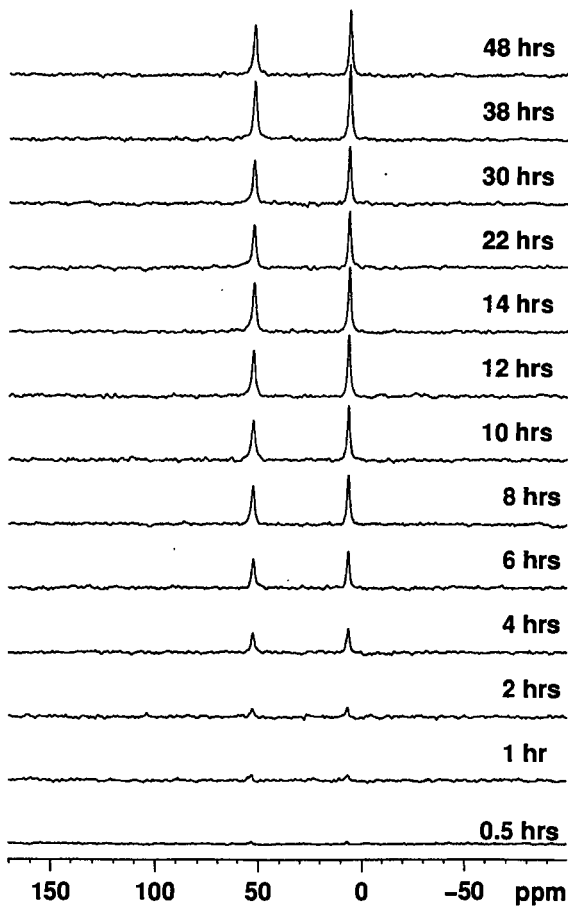


Figure 3. Solid state ^{13}C NMR of the CH_3 - and $-\text{CH}_2$ - TEA peaks during crystallization of TEA-hectorite (ex situ).

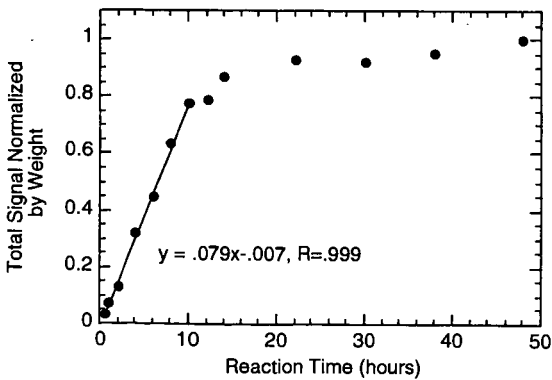


Figure 4. Correlation of TEA ^{13}C NMR signal intensity vs. reaction time during the crystallization of TEA-hectorite.

X-RAY STUDIES OF METAL – SUPPORT INTERACTIONS IN CATALYSTS

J. Lynch, O. Ducreux, D. Uzio, B. Rebours
Institut Français du Pétrole
1 & 4 Avenue de Bois Préau
92852 Rueil Malmaison Cedex
France

KEYWORDS : EXAFS, X-ray diffraction, catalysts

INTRODUCTION

The support plays a number of roles in supported metal heterogeneous catalysts. Besides assuring mechanical integrity of the system it must have an open pore structure providing access to the active phase and may also be an active component through its surface acid properties. The support may also directly affect the properties of the metal phase through what is usually classed as 'metal – support interaction'.

In the case of cobalt catalysts for the Fischer–Tropsch reaction, with metal particles several tens of nanometers in diameter, many supports have been compared. Varying conclusions have been drawn as to the effect of the support on the activity and selectivity of these catalysts. Although in a study by Bartholomew [1] the catalytic activity of supported cobalt varied in the order $\text{Co/TiO}_2 > \text{Co/SiO}_2 > \text{Co/Al}_2\text{O}_3$, Bessel [2] obtained a higher activity for alumina support than for silica while Iglesia et al. [3] found no effect on changing the support. Different activation and operating conditions were however used for these studies. Little information is available on how the support and the activation procedure influences the structure of the cobalt which forms the active phase of this type of catalyst.

The activity of alumina supported palladium catalysts, used for selective hydrogenation reactions, has been shown to reach an optimum for particle sizes of about two nanometers [4]. Although particle sizes below two nanometers would allow an increase in available surface palladium, a decrease in catalytic activity is observed. This has been attributed [5] to the loss of metallic character of the palladium atoms due to an increased effect of the metal–support interaction for small particles. Recent studies in our laboratory show that using palladium nitrite rather than the conventional palladium acetylacetonate as precursor can lead, for palladium particles of the same size, to increased catalytic activity for sub-nanometer particles. It is therefore of interest to determine the possible differences in metal–support interaction induced by changes in the precursor.

One of the major obstacles in obtaining this type of information resides in the fact that the catalysts must be studied in their reduced state. In this study the effect of the metal–support interaction on the structure of the metallic phase has been studied using two in-situ X-ray techniques : X-ray diffraction (XRD) and Extended X-ray Absorption Fine Structure (EXAFS) spectroscopy. The former is well adapted to the case of Fischer–Tropsch catalysts with a large particle size. For the small particles and metal loadings below 1% typical of hydrogenation catalysts no lines due to the metal are observed by XRD. EXAFS is particularly useful in this case as the technique is element specific and no long range order is required.

MATERIALS AND METHODS

Fischer–Tropsch catalysts were prepared by incipient wetness impregnation of TiO_2 , SiO_2 and Al_2O_3 using aqueous solutions of cobalt nitrate. The samples were dried in air and calcined at 573 K before characterisation. XRD showed that the only crystalline form of cobalt present was Co_3O_4 and the corresponding particle sizes were determined by line broadening. Details of cobalt loading, specific surface area and Co_3O_4 particle size are given in table 1.

Catalyst	Co loading (% wt.)	Specific surface area (m^2/g)	Co_3O_4 particle size (nm)
Co/TiO_2	11.3	16	75
Co/SiO_2	13.0	460	14
$\text{Co/Al}_2\text{O}_3$	10.5	180	20

Table 1 : Characteristics of the cobalt catalysts

Supported palladium catalysts with a metal loading of 0.3 % wt. were prepared by incipient wetness impregnation of alumina ($130 \text{ m}^2/\text{g}$) using palladium bis-acetylacetonate in toluene (this solid is referred to as Pd[acac.]) or a mixture of palladium nitrate and sodium nitrite with a 1:4

molar ratio of Pd/NO₂ (referred to as Pd[NO₂]). After drying the solids were calcined at 623K. Transmission electron microscopy studies showed no evidence for particle sizes greater than 1 nm in both cases.

XRD studies of Co/SiO₂ and Co/Al₂O₃ were carried out using Cu (K α) radiation on a Siemens D501 $\Theta - 2\Theta$ powder diffractometer equipped with an Anton Parr reaction chamber adapted to allow Fischer-Tropsch reactions to be carried out [6]. Reduction studies were carried out under hydrogen flow, ramping the temperature up to the desired value at 5K/min then keeping the temperature stable during XRD analysis (4 hrs). CO conversion data was obtained in-situ at 473K using synthesis gas (H₂/CO = 9, 3 bar, 8.5 g.h.l⁻¹). The silica support is amorphous allowing the XRD pattern due to cobalt phases to be clearly identified. For the poorly crystallised alumina sample an XRD pattern of the support without cobalt was subtracted after normalisation. In the case of Co/TiO₂ the presence of many sharp lines from the support (rutile and anatase forms) prevents the cobalt phases from being correctly analysed. This sample was studied using the anomalous diffraction effect at the Laboratoire pour l'Utilisation de Rayonnement Electromagnétique (LURE, Orsay) on the H10 beam line using synchrotron radiation from the DCI storage ring running at 1.85 GeV with an average current of 250 mA. The difference pattern of XRD data recorded at energies far from (7614 eV) and close to (7715 eV) the cobalt K edge allowed the cobalt phases to be isolated.

EXAFS data for the Pd catalysts were obtained on the EXAFS4 beam line at LURE, in transmission mode through a double crystal Si(111) monochromator using two ion chambers as detectors. The EXAFS reactor cell, identical to that designed by Lytle et al. [7], allows *in situ* treatment of samples at temperatures up to 773 K. The sample was reduced under flowing hydrogen using a temperature program (5K/min). The Pd K-edge region was analysed using a standard data analysis package [8]. For analysis of local environment, the EXAFS was first transformed from k space to r space (k³, Hamming windows 2.8, 4.3, 11.3, 12.7 Å⁻¹) to obtain the radial distribution function (RDF). The EXAFS spectrum for the first co-ordination shells was isolated by inverse Fourier transform of the RDF over the appropriate region and fitted using the single scattering EXAFS equation. Amplitude and phase functions for fitting Pd-O and Pd-Pd shells were obtained respectively from Pd(acac) and Pd metal foil references.

Pd catalysts were tested for buta-1.3-diene hydrogenation in a laboratory batch reactor at 10 bar, 290K with gas chromatography analysis of products.

RESULTS

a) cobalt catalysts

Reduction of the Co₃O₄ phase under hydrogen proceeds via the formation of CoO to the formation of metallic cobalt [6]. The XRD pattern after reduction at 773K shows the presence of both fcc and hcp forms of cobalt. Comparing the XRD patterns of the Co/SiO₂ and Co/Al₂O₃ catalysts at a 673K (figure 1) shows that the degree of reduction differs for the different supports.

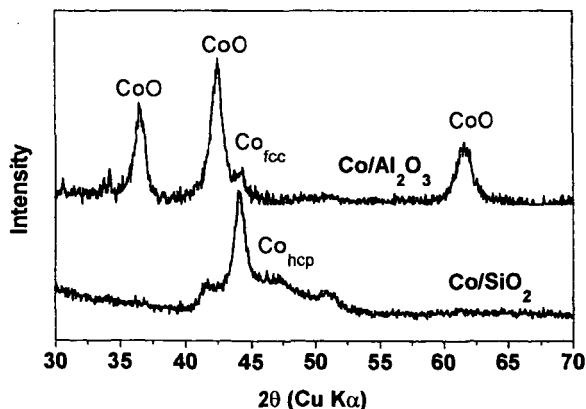


Figure 1 : In-situ XRD patterns of Co/SiO₂ and Co/Al₂O₃ at 673K under hydrogen

The silica supported catalyst is more strongly reduced at 673K than the $\text{Co}/\text{Al}_2\text{O}_3$ sample. This is in agreement with temperature programmed reduction studies showing that Co/SiO_2 is fully reduced at this temperature whereas $\text{Co}/\text{Al}_2\text{O}_3$ shows (as does Co/TiO_2) hydrogen consumption up to much higher temperatures.

The support also has an influence on the relative intensities of the diffraction peaks corresponding to the two forms of metallic cobalt (figure 2). The samples in which the cobalt is reduced only at higher temperatures show an increased proportion of fcc structure compared to hcp cobalt.

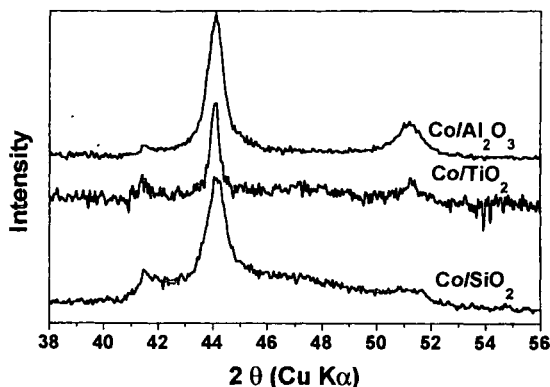


Figure 2 : XRD patterns of the cobalt catalysts reduced at 873 K

Carrying out the Fischer-Tropsch reaction in the XRD cell showed a CO conversion at 50 hrs time on stream of 25% for Co/SiO_2 whereas those of $\text{Co}/\text{Al}_2\text{O}_3$ and Co/TiO_2 were 15% and 14% respectively. On the working hypothesis that the reduction temperature was related to the cobalt microstructure developed, protocols were developed to modify the reduction temperature for a given support. By heating the calcined samples in nitrogen it was possible to stabilise the CoO form on silica at high temperature (823 K). Introducing hydrogen at this temperature provoked the reduction of CoO to metallic cobalt. It was indeed found that reduction at high temperature led to the preferential formation of fcc form. A lowering of the reduction temperature was achieved by adding ruthenium to Co/SiO_2 (impregnation of the calcined sample with ruthenium nitrate in aqueous solution to a loading of 0.3% wt). This sample was found to be fully reduced at 673 K with a majority of hcp cobalt. Figure 3 compares the structures obtained for Co/SiO_2 using these two protocols with that obtained by reduction under hydrogen. Modifying the temperature at which the metallic cobalt is formed clearly leads to controlled variation of the microstructure.

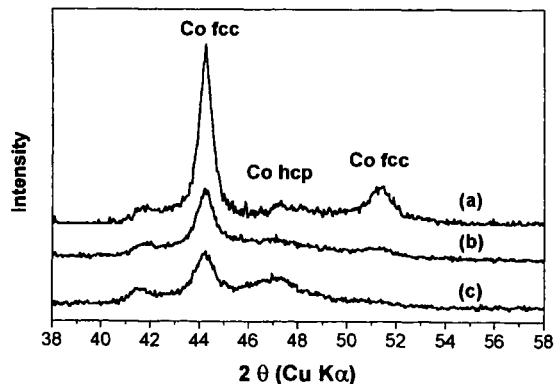


Figure 3 : Comparison of cobalt forms for Co/SiO_2 for (a) high, (b) medium and (c) low temperature reduction protocols.

Activities for the conversion of CO in the Fischer-Tropsch reaction of Co/SiO₂ samples containing different fcc/hcp ratios were significantly different. Promoted Co/SiO₂ (with a high hcp component) showed a two-fold gain in activity compared with Co/SiO₂ whereas the high temperature fcc form showed a two-fold reduction in CO conversion.

b) palladium catalysts

After reduction the sample Pd[NO₂] shows an EXAFS spectrum very similar to Pd metal foil, but of reduced intensity (figure 4). Modelling of the filtered data (inverse Fourier transform window : 1.5 to 3.0 Å) allows the average number of first nearest neighbours to be estimated as 5 +/-1, consistent with the existence of particles less than one nanometer in diameter.

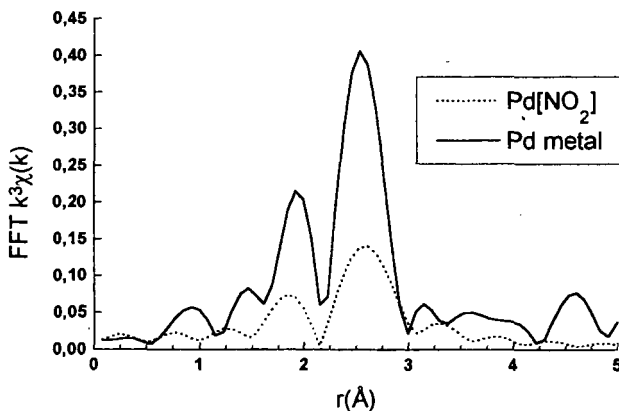


Figure 4 : RDF of the Pd[NO₂] catalyst compared to that of a Pd metal foil

The RDF of the Pd[Acac] sample is compared with that of Pd[NO₂] in figure 5. The Fourier transformed data clearly shows, in addition to Pd-Pd neighbours, a peak at low distances for Pd[Acac]. Modelling of the filtered data (inverse Fourier transform window : 0.95 to 3.0 Å) reveals this peak to be due to oxygen atoms, the average Pd-O co-ordination number being three at a distance of 1.95Å. Pd-Pd co-ordination is similar so that particle size can be considered practically unchanged.

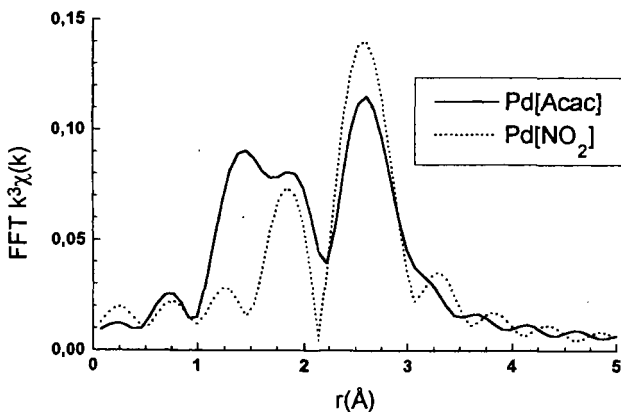


Figure 5 : Comparison of RDFs of the Pd[NO₂] and Pd[Acac] catalysts.

Buta-1,3-diene hydrogenation tests showed that the activity of the Pd[NO₂] catalysts for conversion to butene, 14 mole/min/g(Pd), was over ten times that of the Pd[Acac] catalysts, 1.2 mole/min/g(Pd), with an activity per surface Pd atom close to that obtained by Boitiaux et al. [4] for large palladium particles.

DISCUSSION

In the case of cobalt based Fischer-Tropsch catalysts the support clearly influences both the reducibility of the precursor oxide and the structure of the metal phase obtained after reduction. Our study shows that these effects are linked, and that it is the temperature of reduction that determines the fraction of different cobalt structures in the active catalyst. Modification of the reduction temperature by stabilising the intermediate oxide to high temperatures or by adding a promoter to induce reduction at low temperature enables the microstructure to be controlled. Thus, although it is not yet clear how the various oxide supports influence the temperature of reduction, the parameters controlling the activity of the final catalyst should probably be considered in the light of an oxide-support rather than a metal-support interaction. The catalytic results show that differing ratios of the two cobalt phases, fcc and hcp, lead to differing activities in the conversion of CO. Further work is required to investigate whether the differences can be attributed to intrinsic activities of the two phases or if, as suggested by Srinivisan et al. [9], it is the presence of defects induced by the presence of stacking faults in the cobalt particles that generates the active sites.

The X-ray absorption results for the Pd[NO₂] sample show the palladium in reduced samples to be in an environment close to that of bulk metallic palladium. Although the Pd-Pd co-ordination number is reduced due to the small particle size, no evidence of a well defined particle-support interaction is observed. It is clear on the contrary that the palladium in the Pd[acac] sample is in strong interaction with the support. Comparison of the catalytic results of the two systems clearly demonstrates that for conventional methods of preparation it is the metal-support interaction which leads to a reduction of activity in the case of small particles. The small Pd[NO₂] particles show similar activity to large particles for which the metal-support interaction would be diluted.

CONCLUSIONS

In-situ XRD and EXAFS have allowed the microstructure of catalysts in the active state to be characterised and give an insight into the parameters controlling the activity of the metallic phase. In the case of large cobalt particles, XRD shows differences in microstructure as a function of the support that can be rationalised in terms of reduction temperature. This has allowed protocols to be defined that lead to controlled microstructures whose presence can be directly correlated to activity in Fischer-Tropsch synthesis. EXAFS studies of small palladium particles demonstrate that the activity of hydrogenation catalysts can be clearly linked to the presence or absence of metal-support interaction. Control of this interaction can lead to higher activities for small particles and thus to more efficient catalysts.

ACKNOWLEDGEMENTS

This work was partly supported by a grant from the European Union (contract N° JOF3-CT95-0016). The authors are grateful to D. Bazin and M. Gaillanou (L.U.R.E., Orsay) for assistance in EXAFS and anomalous XRD experiments.

REFERENCES

- 1 C. H. Bartholomew, *Catal. Lett.*, **7**, (1990), 27-52
- 2 S. Bessel, *Appl. Catal.*, **96**, (1993) 253-268
- 3 E. Iglesia, S. L. Soled and R. A. Fiato, *J. Catal.*, **137**, (1992) 212-224
- 4 J. P. Boitiaux, J. Cosyns, E. Robert, *Appl. Catal.*, **345**, (1987) 193-209
- 5 J. C. Bertolini, P. Delichère, B. C. Khandra, J. Massardier, C. Noupa and B. Tardy, *Catal. Lett.*, **6**, (1990) 215-224
- 6 O. Ducreux, J. Lynch, B. Rebours, M. Roy, P. Chaumette, *Studies in Surf. Sci. and Catalysis*, **119**, (1998) p. 125-130
- 7 F. W. Lytle, G.H. Via and J. H. Sinfelt, in *Synchrotron Radiation Research*, eds. H. Winick and S. Doniach, Plenum Press, New York, 1980, 401-424
- 8 A. Michalowicz A., *J. Phys. IV*, **7**, (1997), C2-235-236
- 9 R. Srinivisan, R. J. de Angelis, P. J. Reucroft, A.G. Dhere and J. Bently, *J. Catal.*, **116**, (1989) 144-163

CHARACTERIZATION OF NANOSTRUCTURED ZIRCONIA PREPARED BY HYDROLYSIS AND REVERSE MICELLE SYNTHESIS BY SMALL-ANGLE NEUTRON AND X-RAY SCATTERING

P. Thiyagarajan¹, X. Li^{1,4}, K.C. Littrell¹, S. Seifert², R. Csencsits³, and C.K. Loong¹.
¹Intense Pulsed Neutron Source, ²Chemistry Division, ³Materials Science Division Argonne National Laboratory, 9700 South Cass Avenue, Argonne, IL 60439,
⁴Chemical Engineering Department, University of Louisville, Louisville, KY 40292.

Keywords: Nanophase Zirconia, Reverse Micelle Synthesis, Small angle neutron and x-ray scattering

ABSTRACT

Low temperature techniques such as hydrolysis and reverse micelle syntheses provide the opportunity to determine the relationship between the structural properties and preparation conditions of zirconia powders as well as to tailor their physicochemical properties. We have performed small-angle neutron and synchrotron x-ray scattering (SANS and SAXS) experiments to study the nucleation and organization of zirconia nanoparticles via different preparation routes. First, the formation of reverse micelles in individual and mixed solutions of $(\text{ZrOCl}_2 + \text{D}_2\text{O})/\text{AOT}/\text{C}_6\text{D}_6$, and $(\text{NH}_4\text{OH} + \text{H}_2\text{O})/\text{AOT}/\text{C}_6\text{D}_6$ systems at water/AOT molar ratio of 20 was characterized. Second, the aggregation of zirconia gels obtained from the reaction of the reverse micelle solutions after heat treatments was studied. Third, the nanostructure of zirconia powders prepared by the reverse micelle method is compared with the corresponding powders prepared by hydrolysis after different heat treatments.

INTRODUCTION

Zirconia based materials are widely used as catalysts and catalytic supports by the automobile industry for the automobile-exhaust emission control. These materials offer unique combination of properties such as high surface area, good thermal stability and rich site activity. They can be prepared by a variety of novel preparation methods such as hydrolysis, sol-gel and reverse micelle synthesis. We have demonstrated that doping of zirconia with certain rare earth oxides significantly alter its microstructure and enhance its thermal stability¹. Recently, we have also investigated the structural features of a series of AOT/H₂O/toluene reverse micelle solutions in the presence of reactants for the synthesis of zirconia nanoparticles by SANS².

The nanostructure of the zirconia powder and its thermal stability are closely related to the synthetic conditions used in the solution phase. To gain a better understanding of the structure and function relationship of zirconia we have prepared zirconia by an hydrolysis method at pH = 9.8 and a reverse micelle method in AOT/H₂O/toluene at water/AOT ratio $w = 20$. The obtained gels were calcined at 580 °C for 2 hours in order to remove the residual hydrocarbons and water. The SEM and TEM images of the calcined zirconia powders prepared by the hydrolysis and reverse micelle methods are shown in Figs. 1A and 1B, respectively. It can be seen that the particle size in the zirconia powder from hydrolysis method is in the micrometer range, while it is in the nanometer range from the reverse micelle synthesis. Thus controlled environment used in the reverse micelle method significantly affects the nanostructure of the particles in the zirconia powder.

While TEM provides direct images of the particles in the zirconia powder, the small angle scattering techniques with either neutrons (SANS) or x-rays (SAXS) can characterize the organization of the fundamental structural units in gels, powders and solutions. The latter techniques have high sensitivity to structural features in the length scale of 1 to 50 nm. Our objectives in the present study are: 1) to obtain a structure of the particles in the solution phases used in the hydrolysis and reverse micelle methods for the zirconia synthesis by using SANS, 2) to compare the structure of the reverse micelles in deuterated toluene from SANS and that in n-heptane from SAXS at $w = 20$, and 3) to investigate the systematic changes in the nanostructure of zirconia powders prepared by the two techniques as a function of heat treatment.

MATERIALS AND METHODS

In the hydrolysis method a zirconium hydroxide gel was prepared by the addition of an aqueous ammonia solution to an aqueous solution of 0.2 M zirconium oxychloride under continuous vigorous stirring. Solutions were prepared at pH = 9.8 and the pH was adjusted by using 25 wt.% NH₄OH (Alfa) stock solution. The precipitate was washed with water and filtered several times until no Cl⁻ was detected in the filtrate. The gel was dried at 120 °C for 5 hours followed by calcination at 580 °C in the air to obtain the zirconia powder.

Equation 3 has been derived from model for mass-fractal aggregates⁵ of spheres of radius R , given by

$$I(Q; \xi, D_f, R) = I_{0s} \left(1 + \frac{\sin[(D_f - 1)\arctan(Q\xi)]}{(QR)^D \left(\frac{1}{Q^2\xi^2} + 1 \right)^{\frac{D-1}{2}}} \right) P_{\text{Sphere}}(Q; R) + I_{\text{Background}}, \quad (4)$$

where I_{0s} is the intensity scattered by the fundamental spherical particle extrapolated to $Q = 0$. I_{0A} is related to I_{0s} by the expression

$$I_{0A} = I_{0s}(D_f - 1) \Gamma(D_f - 1) \left(\frac{\xi}{R} \right)^{D_f}. \quad (5)$$

This model is a valid approximation when the scattering from the form factor for the fundamental sphere is not visible or, alternately, whenever $\xi \gg R$ and $Q_{\text{max}}R \ll 1$, where Q_{max} is the value of Q at which the power-law scattering fades into the background scattering.

RESULTS AND DISCUSSION

SANS data for the reverse micelles of AOT containing D_2O , $ZrOCl_2$, NH_4OH - D_2O and Zirconia in D-toluene on absolute scale are presented in Fig. 2A. For clarity of presentation the data for the above systems were multiplied by 1, 0.1, 10 and 3, respectively. Similarly scaled SAXS data of AOT containing H_2O , $ZrOCl_2$, NH_4OH and zirconia in n-heptane are in Fig. 2B. The important features in the SANS data are the secondary peaks whose maxima occur at different Q values. In the case SAXS data the secondary peaks are not prominent.

SANS data of the reverse micelles were fitted by using equation 1 to obtain the information on the scattering length density of the core and the results are shown in Table 1. The size of the water core of AOT reverse micelles in D-toluene at $w = 20$ is influenced by its constituents. In the presence of D_2O the core radius is 18 Å with a rms spread of 4 Å, while it decreases to 8 Å in the presence of NH_4OH . The shell thickness remains around 12 Å, except for the micelle with NH_4OH . It is interesting to note that α varies from -1.43 to 0.04 consistent with the composition changes in the core. The effect of the small α values for the NH_4OH and zirconia reverse micelles can be seen in the blurred secondary peaks in the SANS data (Fig. 2A). Another important feature seen for the zirconia containing reverse micelle is the power-law scattering of $Q^{-2.16}$ in the low Q region, implying the presence of vesicles⁶.

SAXS data in Fig. 2B were modeled by using equation 1 to obtain the core radius, shell thickness and α and the results are given in Table 2. SAXS data show that the core radius is larger for the micelle with water, but it becomes smaller for the other cases. The solvent effect is significant on the size of the AOT/water reverse micelles at $w = 20$ as the radius is about 42 Å in n-toluene (SAXS) while it is 30 Å in D-toluene (SANS). Comparison of the SANS data of AOT/water reverse micelles at $w = 20$ in D-toluene and the SAXS data of reverse micelles in n-heptane indicate the strong effect of organic solvent on the reverse micelles size. This is consistent with the fact that the solvent-solute interactions in the aromatic solvents with π electrons will be stronger than that in the aliphatic solvents.

SANS data for the heat-treated zirconia powder samples from the hydrolysis and reverse micelle methods are shown in Figs. 3A and 3B. The presence of peaks in Fig. 3A implies that the zirconia particles are organized at specific distances and the movement of peak positions (Q_{max}) indicates that the particles grow with increasing temperature (Table 3). The approximate particle size ($2\pi/Q_{\text{max}}$) at 300 °C is 60 Å and grows to 423 Å at 800 °C. The power-law slope in the high Q region reaches a value of -4 at 800 °C implying that the surface of the particles became smooth.

SANS data for the zirconia powder prepared from the reverse micelle method are shown in Fig. 3B. This data exhibit power-law scattering Q^{-D} behavior in a wide Q region, but have no peaks. In the case of fractal aggregates the power-law exponent values can be used to identify the mass and surface fractals. For example, mass fractal aggregates will have $1 < D < 3$, while the surface fractals will have $3 < D < 4$. The data were fitted by using equation 3 and obtained the mass fractal dimensions that vary in the range of 2.7 to 2.9 and the cut-off lengths vary in the range of 180 to 340 Å (see Table 4). Thus the zirconia from the reverse micelle method would be better for the high temperature applications than that from the hydrolysis method.

The details of the synthesis of zirconia by the reverse micelle method have been presented elsewhere². Briefly, sodium bis(2-ethylhexyl) sulphosuccinate (AOT) was dissolved in toluene to form a 0.1 M solution. Deionized water was then added to form the reverse micelle with [water]/[AOT] molar ratio $w = 20$. To obtain the Zr-containing reverse micelles, appropriate amounts of 0.2 M $ZrOCl_2$ stock solution corresponding to $w = 20$ was added to the AOT/toluene solution. Similarly, ammonium hydroxide was added to AOT/toluene solution to achieve $w = 20$. All solutions were stirred continuously during the formation of reverse micelles. Subsequently, the Zr- and ammonium-containing solutions of the same w value were mixed and stirred for 20 minutes at room temperature to ensure equilibrium.

SANS experiments were carried out at the time-of-flight small-angle neutron diffractometer (SAND) at the Intense Pulsed Neutron Source of Argonne National Laboratory. This instrument provides a useful range of wave vectors ($Q = 4\pi\sin(\theta)/\lambda$, where θ is half the scattering angle and λ is the neutron wavelength) of $0.0035 - 0.6 \text{ \AA}^{-1}$ in a single measurement. In order to obtain the best contrast for SANS, D_2O (Alfa) and $C_6D_5CD_3$ (Alfa, 98% D-atom) were used. The following four systems, $D_2O/AOT/C_6D_5CD_3$, $ZrOCl_2$ in $D_2O/AOT/C_6D_5CD_3$, NH_4OH in $AOT/C_6D_5CD_3$ and $ZrOCl_2$ reacted with NH_4OH in $AOT/C_6D_5CD_3$ were considered for the present study. The data were corrected following routine procedures³.

SAXS experiments on AOT/ H_2O/n -heptane solutions at $w = 20$ were carried out at the ASAXS instrument on the BESSRC ID-12 beam line at the Advanced Photon Source⁴ also at Argonne National Laboratory. Data were collected using a position sensitive $15 \text{ cm} \times 15 \text{ cm}$ CCD area detector and exposure times for each measurement were 1 - 2 seconds. A known quantity of a solution was injected into a flow cell using motorized syringes that can position the sample into the 1.5 mm diameter cylindrical capillary tube viewed by the x-ray beam. The sample to detector distance was 0.7 m and the energy of x-ray radiation was set at 13.5 keV.

DATA ANALYSIS

The SAS data from the reverse micelle samples were analyzed by using the core-shell model given in equation 1. In this equation the variables, r , T and α are the core radius, thickness and the ratio of scattering length density difference between the core and shell to that between the shell and the solvent, respectively. The neutron scattering length densities of D_2O , AOT and D-toluene are $6.336 \times 10^{10} \text{ cm}^{-2}$, $0.62 \times 10^{10} \text{ cm}^{-2}$ and $5.644 \times 10^{10} \text{ cm}^{-2}$ respectively. The x-rays are scattered by the electrons and the scattering length densities of H_2O , AOT and n-heptane are $9.36 \times 10^{10} \text{ cm}^{-2}$, $10 \times 10^{10} \text{ cm}^{-2}$ and $6.64 \times 10^{10} \text{ cm}^{-2}$ respectively. The scattered intensity can be expressed as

$$I(Q) = nP(Q)S(Q) \quad (1)$$

where n is the number density of the reverse micelles, $P(Q)$ is the form factor and $S(Q)$ is the inter-particle structure factor which is assumed to be 1 in this case. The form factor $P(Q)$ for a spherical shell with a polydispersity in radius with Shultz distribution is given by

$$P(Q) = \frac{\int_0^{\infty} [\sin(Q(r+T)) - Q(r+T)\cos(Q(r+T)) + \alpha(\sin(Qr) - Qr\cos(Qr))]^2 \left(\frac{r}{r_0}\right)^{x-1} \exp\left(-\frac{zr}{r_0}\right) dr}{\int_0^{\infty} [(r+T)^3 + \alpha^2] \left(\frac{r}{r_0}\right)^{x-1} \exp\left(-\frac{zr}{r_0}\right) dr} \quad (2)$$

where

$$\alpha = \frac{\rho_{\text{core}} - \rho_{\text{shell}}}{\rho_{\text{shell}} - \rho_{\text{solvent}}}, \quad \text{and} \quad z = \frac{r_0}{\sigma}$$

where σ is the rms core radius spread.

The SANS from the zirconia powders are fitted by using equation 3 for fractal aggregates⁵.

$$I(Q, \xi, D_f) = I_{0A} \frac{\sin[(D_f - 1)\arctan(Q\xi)]}{(D_f - 1)Q\xi(Q^2\xi^2 + 1)^{\frac{D_f - 1}{2}}} + I_{\text{background}} \quad (3)$$

where I_{0A} is the overall intensity scattered by the aggregate extrapolated to $Q = 0$, D_f is the mass-fractal dimension, ξ is the exponential cutoff length at which the system reaches the macroscopic density, and $I_{\text{background}}$ is the background intensity.

CONCLUSIONS

SAXS and SANS are quite sensitive for the study of the nanostructure of catalytic systems. The high sensitivity of the scattering techniques can be seen from their ability to provide a number of parameters on the structure and organization of the reverse micelles. We obtained unique information on the water core that provides clues to the enhanced properties of zirconia. Coarsening occurs in zirconia powder prepared by hydrolysis method upon heat treatment, while the particles are uniform in size and do not grow upon heat treatment up to 750 °C.

ACKNOWLEDGEMENTS

This work was performed under the auspices of the Office of Basic Energy Sciences, Division of Chemical and Materials Sciences, U.S. Department of Energy, under contract number W-31-109-ENG-38. We are indebted to Randall Winans, Chemistry Division for his effort in setting up the SAXS instrument at BESSRC. The support of Jennifer Linton, Guy Jennings and Mark Beno at BESSRC and Denis Wozniak at IPNS is appreciated.

REFERENCES

1. Loong, C.K.; Thiyagarajan, P.; Richardson Jr., J.W.; Ozawa, M.; Suzuki, S. J. Catalysis 1997, 171, 498-505.
2. Li, X.; Loong, C.-K.; Thiyagarajan, P.; Lager, G.A.; Miranda, R. J. Appl. Cryst. (In Press).
3. Thiyagarajan, P.; Epperson, J.E.; Crawford, R.K.; Carpenter, J.M.; Klippert, T.E.; Wozniak, D.G. J. Appl. Cryst. 1997, 30, 280-293.
4. Seifert, S.; Winans, R.E.; Tiede, D.M.; Thiyagarajan, P. J. Appl. Cryst. (In Press)
5. Freltoft, T.; Kjems, J.; Sinha, S.K. Phys. Rev. 1986, B33, 269.
6. Ravey, J.C.; Buzier, M. J. Colloid. Interface Sci., 1987, 116, 30.

Table 1
Parameters from the Shultz Polydisperse Shell model fits of SANS of Reverse Micelles of AOT/D₂O in D-Toluene, w = 20.

Core in AOT/ D-Toluene Reverse Micelle	Core radius (Å)	RMS Core Radius Spread (Å)	Shell thickness (Å)	$(\rho_{\text{core}} - \rho_{\text{shell}}) /$ $(\rho_{\text{shell}} -$ $\rho_{\text{solvent}})$ (α)	ρ_{core} (10^{10} cm^{-2})
D ₂ O	18.0 ± 0.1	4.0 ± 0.1	12.0 ± 1.0	-1.143	6.36
ZrOCl ₂	10.1 ± 0.7	1.6 ± 0.2	12.0 ± 0.8	-1.019	5.73
NH ₄ OH	8.4 ± 0.4	2.3 ± 0.4	14.1 ± 0.4	-0.051	0.88
ZrO ₂	12.0 ± 2.0	2.6 ± 0.1	11.0 ± 2.0	0.040	0.42

Table 2
Parameters from the Shultz Polydisperse Shell model fits of SAXS of Reverse Micelles of AOT/H₂O in n- heptane, w = 20.

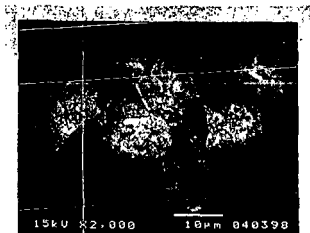
Core in AOT/ n-heptane Reverse Micelle	Core radius (Å)	RMS Core Radius Spread (Å)	Shell thickness (Å)	$(\rho_{\text{core}} - \rho_{\text{shell}}) /$ $(\rho_{\text{shell}} -$ $\rho_{\text{solvent}})$ (α)	ρ_{core} (10^{10} cm^{-2})
H ₂ O	30.7 ± 0.01	8.5 ± 0.01	11.3 ± 0.05	-0.328	8.90
ZrOCl ₂	11.0 ± 0.01	3.9 ± 0.01	10.7 ± 0.06	-0.520	8.25
NH ₄ OH	24.4 ± 0.01	7.8 ± 0.01	12.0 ± 0.1	-0.386	8.70
ZrO ₂	27.2 ± 0.01	8.2 ± 0.01	12.0 ± 0.1	-0.375	8.74

Table 3
Particle size from the SANS data of the zirconia powders prepared by the hydrolysis method upon heat treatment for 2 hours at different temperatures.

Temp. (°C)	Particle Size (Å)
300	60
400	90
500	134
600	203
700	295
800	423

Table 4
Parameters obtained from the Fractal model fit of the SANS data of the zirconia powders prepared using reverse micelle method upon heat treatment for 2 hours at different temperatures.

Temp (°C)	Fractal Dimension	Cutoff Length (Å)
100	2.7	186
200	2.7	197
300	2.7	148
400	2.9	124
550	2.93	223
750	2.9	341



(A)



(B)

Fig. 1. A) STM of calcined Zirconia powder prepared by hydrolysis method B) TEM of calcined zirconia powder prepared by reverse micelle method with H_2O/AOT $w=20$.

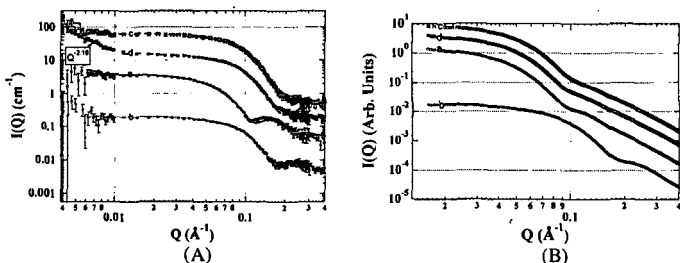


Fig. 2 A) SANS of reverse micelle solutions at $w = 20$: (a) $D_2O/AOT/C_6D_5CD_3$, (b) $(ZrOCl_2+D_2O)/AOT/C_6D_5CD_3$, (c) $(NH_4OH+H_2O)/AOT/C_6D_5CD_3$, and (d) the mixture of (b) and (c). B) SAXS of reverse micelle solutions at water/AOT molar ratio = 20: (a) $H_2O/AOT/C_7H_{16}$, (b) $(ZrOCl_2+H_2O)/AOT/C_7H_{16}$, (c) $(NH_4OH+H_2O)/AOT/C_7H_{16}$ and (d) mixture of (b) and (c). For clarity, the absolute intensities of data a, b, c and d are multiplied by 1, 0.1, 10 and 3, respectively. Lines are the fits using equation 1 and the results from the fits of SANS and SAXS data are given in Tables 1 and 2, respectively.

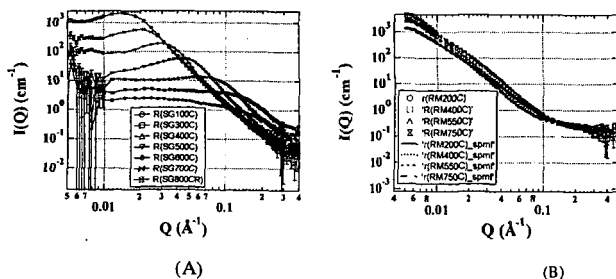


Fig. 3 SANS of ZrO_2 powders prepared by A) hydrolysis and B) reverse micelle synthesis after heat treatment at different temperatures for 2 hours. While the aggregates in ZrO_2 powders prepared by hydrolysis method shows monotonic increase in their size, those in ZrO_2 powders from reverse micelle method seem to be stable up to 750 °C.